DOI:10.12119/j.yhyj.202203003

Performance and Mechanism of Recovering Lithium from Aqueous Solution by Spherical $MnO_2 \cdot 0.5H_2O$

ZHANG Guo-tai[1,2], QI Gui-cai[1,2], HAI Chun-xi[1,*], ZHOU Yuan[1,*]

(1. *Key Laboratory of Comprehensive and Highly Efficient Utilization of Salt Lake Resources, Key Laboratory of Salt Lake Resources Chemistry of Qinghai Province, Qinghai Institute of Salt Lakes, Chinese Academy of Sciences, Xining*, 810008, *China*; 2. *University of Chinese Academy of Sciences, Beijing*, 100049, *China*)

Abstract: The influence of morphology on the adsorption capacity of spinel-structured $MnO_2 \cdot 0.5H_2O$ lithium ion-sieves (LISs) prepared by the treatment of a $Li_{1.6}Mn_{1.6}O_4$ precursor in HCl was experimentally investigated. The obtained samples were characterized by X-ray diffraction (XRD), scanning electron microscopy (SEM), transmission electron microscopy (TEM), Fourier-transform infrared spectroscopy (FT-IR), X-ray photoelectron spectroscopy (XPS), and N_2 adsorption-desorption isotherms. Spherical LISs were demonstrated to have a higher adsorption capacity (up to 42.46 mg/g) and selectivity toward Li^+ in solution than their cubic counterparts. As a result, the morphology of reactant Mn_2O_3 was determined to largely determine the morphology of the precursor prepared by a typical two-step solid-phase reaction and its corresponding adsorbent. Additionally, the results presented here indicate that both surface deprotonation and ion-exchange processes of the as-prepared sieve-type adsorbent contribute to its enhanced Li^+ adsorption performance.

Key words: Spinel $Li_{1.6}Mn_{1.6}O_4$; $MnO_2 \cdot 0.5H_2O$; Lithium recovery; Adsorption capacity; Adsorption-desorption mechanism

CLC number: O611.62 **Document code**: A **Article ID**: 1008 - 858X(2022)03 - 0021 - 13

1 Introduction

The soaring demand for high-quality lithium products in recent decades has encouraged researchers to investigate the separation and extraction of lithium from salt lakes, which comprise almost 60% of the global lithium reserves and are thus regarded as an important lithium source[1,2]. However, salt lake brines are also rich in many other metal salts, such as Na^+, K^+, and Mg^{2+}. In particular, the similar ionic radius of Mg^{2+} (0.086 nm) and Li^+ (0.090 nm), the extremely low Li^+ concentration ($50 \times 10^{-6} \sim 1\ 000 \times 10^{-6}$), and high Mg/Li mass ratio (2 ~ 2000) has limited the large-scale production of lithium from low-grade salt lake brines. Various methods have been employed to improve lithium

Received date: 2021 - 05 - 25; **Revised date**: 2021 - 07 - 19

Fund projects: National Natural Science Foundation of China (U20A20337); Natural Science foundation of Qinghai Province (2021 - ZJ - 903); Major science and technology projects of Qinghai Province (2019 - GX - 168)

First author: Zhang Guo - tai (1994 -), male, doctor, mainly engaged in the study of solvent extraction chemistry and chemical engineering. Email: zhangguotai17@mails.ucas.ac.cn

Corresponding author: Hai Chun - xi, PHD, professor, Email: haicx@isl.ac.cn

recovery from salt lake, including solar evaporation[3], co-precipitation[4], adsorption[5], solvent extraction[6], and electrochemical methods[7]. Due to its low cost and relatively simple technique, selective adsorption is believed to be an effective and promising way to recover lithium from an aqueous solution.

Although various adsorbents have been developed to recover lithium via selective adsorption, Mn-based lithium ion-sieves (LISs) have attracted interest due to their ultra-high theoretical adsorption capacity, high selectivity, and good chemical and thermal stability[5,8]. An adsorbent's capacity is determined mainly by the crystal structure (ramsdelite or spinel-type) or surface properties. Further, experimental analyses have demonstrated that only $MnO_2 \cdot xH_2O$ involving λ-MnO_2, $MnO_2 \cdot 0.31H_2O$, and $MnO_2 \cdot 0.5H_2O$ adsorb Li^+ in a solution; the theoretical lithium capacities of λ-MnO_2, $MnO_2 \cdot 0.31H_2O$ and $MnO_2 \cdot 0.5H_2O$ adsorbent are 38.4, 56.4 and 72.3 mg/g, respectively[5,8,9]. As such, increased attention has been given to $MnO_2 \cdot 0.5H_2O$ prepared by the delithiation of precursor $Li_{1.6}Mn_{1.6}O_4$ with a spinel crystal structure. Typically, preparing a $Li_{1.6}Mn_{1.6}O_4$-type LIS requires three steps. Firstly, the $Li_{1.6}Mn_{1.6}O_4$ precursor is prepared via the phase transformation process of monoclinic-structured $LiMnO_2$ prepared by either the hydrothermal reaction of λ-MnOOH with LiOH[10-12] or the solid-phase reaction of Mn_2O_3 and LiOH[13]. Secondly, the sieve function of the $Li_{1.6}Mn_{1.6}O_4$-type LIS adsorbent is activated via ion exchange between the Li^+ in the precursor and the H^+ in the solution with the aid of HCl. The sites where H^+ replaced Li^+ in as-obtained $H_{1.6}Mn_{1.6}O_4$ ($MnO_2 \cdot 0.5H_2O$) have a high affinity toward Li^+ in a Li^+-containing solution, thus providing the $MnO_2 \cdot 0.5H_2O$-type LIS good adsorption capacity. Finally, the precursor $Li_{1.6}Mn_{1.6}O_4$ can be regenerated easily after recovering Li resources in a solution. Repeating these three steps can effectively realize lithium recovery with high efficiency and selectivity in what has been described as the "LIS effect"[14,15]. Several physiochemical properties of precursor $Li_{1.6}Mn_{1.6}O_4$ have been demonstrated to impact the adsorption performance of $MnO_2 \cdot 0.5H_2O$-type LIS, including the crystal structure, morphology, dispensability, specific surface area, and size uniformity. Thus, the structure, morphology, and dispersibility of the $Li_{1.6}Mn_{1.6}O_4$ precursor directly and largely influence the LIS application property.

Chitrakar et al.[16] hydrothermally synthesized fine $LiMnO_2$ particles (approximately 0.1 μm in size) by employing λ-MnOOH as a starting material. Their as-prepared spinel-structured $MnO_2 \cdot 0.5H_2O$ nanospheres had a typical diameter range of 100 ~ 300 nm and a lithium capacity of ≤37 mg/g from Li^+-enriched seawater. Liu et al.[17] discovered that one-dimensional $MnO_2 \cdot 0.5H_2O$ with a nanowire morphology (50 ~ 200 nm in diameter and 0.5 ~ 2 μm in length) exhibits a fairly good adsorption capacity of up to 10.05 mg/g (pH = 10) for Li^+ extraction from seawater. According to their report, high-purity $LiMnO_2$ was prepared by the combination of sol-gel and hydrothermal methods using $Mn(NO_3)_2 \cdot 4H_2O$ as a manganese source. Shi et al.[18] demonstrated a high Li^+ adsorption capacity (up to 27 mg/g) of a $MnO_2 \cdot 0.5H_2O$ absorbent with an average size of approximately 100 ~ 300 nm, prepared by employing Mn_2O_3 as a starting reagent instead of the commonly utilized λ-MnOOH, which loses chemical and structural stability. Accordingly, owing to its higher controllability, using Mn_2O_3 not only simplifies preparation but also allows the $Li_{1.6}Mn_{1.6}O_4$-type precursor to be prepared with controllable parameters[13,17]. Nevertheless, the adsorption capacity of their as-prepared $MnO_2 \cdot 0.5H_2O$-type LIS was limited when compared with its theoretical capacity. Replacing the unstable λ-MnOOH with Mn_2O_3 with its controllable structure and surface properties may thus allow further increases to the adsorption capacity. Further, the preparation of and working mechanism behind sphere-like $MnO_2 \cdot 0.5H_2O$ adsorbents have not yet been examined in detail.

Micro-nanostructured Mn_2O_3 spheres with abun-

dant surface-active sites have been synthesized by a modified polyol method[19]. This work therefore aims to synthesize porous spherical and cubic-like LIS adsorbents. Briefly, benefiting from its higher specific surface area and mesopores, sphere-like LIS has a higher Li^+ adsorption capacity up to 42.46 mg/g than that of cubic-like LIS. Based on the experimental results, an adsorption-desorption mechanism of the as-prepared $MnO_2 \cdot 0.5H_2O$ adsorbent is also proposed.

2 Experimental Section

2.1 Materials and reagents

Manganese(II) chloride tetrahydrate, ammonium hydroxide, ethylene glycol, lithium hydroxide monohydrate, hydrochloric acid, lithium chloride monohydrate, sodium chloride, potassium chloride, calcium chloride and magnesium chloride hexahydrate, purchased from Sinopharm Chemical reagent Co. Ltd., were all analytical grade and all were directly used without any further purification treating.

2.2 Synthesis of $MnO_2 \cdot 0.5H_2O$ lithium ion-sieves

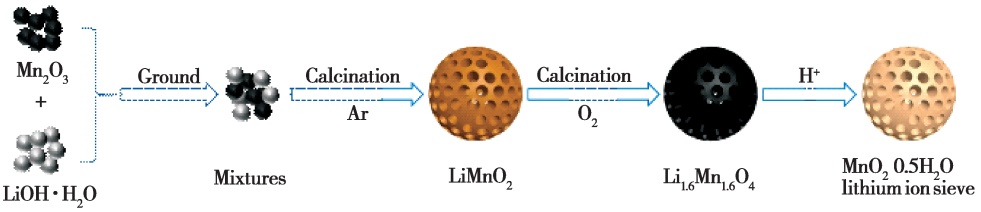

Fig. 1　Schematic of the lithium ion-sieve (LIS) preparation process

Typically, $MnO_2 \cdot 0.5H_2O$ LISs were obtained from the acid treatment of $Li_{1.6}Mn_{1.6}O_4$ precursors that were synthesized by two-step solid-phase methods. Here, LISs were prepared as shown in Fig. 1. Spherical and cubic mesoporous Mn_2O_3 were prepared as detailed by Qi[17]. The as-prepared Mn_2O_3 and commercial $LiOH \cdot H_2O$ were then mixed at a molar ratio (Li/Mn) of 1.08 to avoid the volatilization of lithium at a high temperature. After thoroughly mixing and drying, the as-obtained mixture was calcined at 600 ℃ for 8 h under an Ar atmosphere with a temperature increase rate of 10 ℃/min in a tubular furnace to obtain intermediate $LiMnO_2$. The $Li_{1.6}Mn_{1.6}O_4$ (LMO) precursor was prepared by the oxidation of as-obtained $LiMnO_2$ specimens at 450 ℃ for 6 h under an O_2 atmosphere in a tubular furnace. Finally, 1 g of as-prepared $Li_{1.6}Mn_{1.6}O_4$ precursor was stirred in 250 mL of a 0.5 mol/L HCl solution at 25 ℃ for 9 h, and then filtered, washed, and dried at 80 ℃ for 8 h to obtain the LIS adsorbent. According to the shape differences of the employed Mn_2O_3 reactants, the as-obtained intermediate $LiMnO_2$, LMO precursor, and objective materials, LISs at each preparation step were labeled C-or S-$LiMnO_2$, LMO, and LIS, where C and S represent cubic and spherical, respectively.

2.3 Batch adsorption experiments

10 mg LIS was added into 50 mL 100 mg/L LiOH solutions with different pH values ranging from 2 to 12, and then the solutions were continuously stirred in a shaker with a rate of 100 r/min at 25 ℃ for 48 h. After reaching equilibrium, supernatant samples were collected to examine the concentration of Li^+ by ICP-AES (iCAP6500 DUO, Thermo Fisher Scientific, America). Similarly, 10 mg LIS were added into 50 mL LiCl solutions with different initial Li^+ concentrations (10 ~ 1 000 mg/L) at pH = 12, then stirred (100 r/min, 25 ℃) for 48 h, supernatant samples were taken at intervals to examine the concentration changes of Li^+ by ICP. Furthermore, to perform the recycling utility of LIS, the Li^+-adsorbed LIS were regenerated by stirring in HCl solution (0.5 mol/L) to obtain LMO and then were reused to

capture Li^+ as mentioned above. Selectivity experiment of LIS to Li^+ compared with other co-existing was carried out by stirring 10 mg LIS in 50 mL solution containing 100 mg/L Li^+, Na^+, K^+, Ca^{2+} and Mg^{2+} for 48 h(100 r/min, 25 ℃, pH = 12).

The adsorption capacity Q_t (mg/g) at time t (s), distribution coefficient K_d (mL/g), separation factor($\alpha_{M_e}^{Li}$) and concentration factor C_F (L/g) were calculated according to the following equations(1) – (4)[18].

$$Q_t = \frac{(C_0 - C_t) \times V}{W} \quad (1)$$

$$K_d = \frac{(C_0 - C_e) \times V}{(C_e \times W)} \quad (2)$$

$$\alpha_{M_e}^{Li} = \frac{K_d(Li)}{K_d(M_e)} (M_e = \mathrm{Li, Na, K, Ca, Mg}) \quad (3)$$

$$C_F = \frac{Q_e(M_e)}{C_0(M_e)} \quad (4)$$

where C_0 (mg/L), C_t (mg/L) and C_e (mg/L) are the Li^+ concentration of at initial, adsorption time t and equilibrium stages, respectively. V(mL) is solution volume; W (g) is the weight of LIS. Q_e is the equilibrium adsorption capacity and concentration. M_e indicates Li, Na, K, Ca and Mg, respectively.

2.4 Characterization methods

Crystal structure of as-prepared samples were characterized by X-ray diffraction(XRD, Rigaku D/Max-2200 PC) with Cu Kα-radiation(λ = 1.540598 Å) performed on the samples in the range of 10 ~ 80°. Morphologies of samples were observed by scanning electron microscopy(SEM, Su8010, Hitachi, Japan) and transmission electron microscope (TEM, JEM – 2100, JEOL, Japan). X-ray photoelectron spectroscopy(XPS, EscaLab 250Xi, Thermo Fisher Scientific, America) was used to analyse the surface of samples. Brunauer-Emmett-Teller (BET) gas sorptometry measurements and Barrett-Joyner-Halenda(BJH) methods were conducted on Autosorb-iQ2-MP at 77 K to examine the porous nature and pore size distribution. Before measurements, all samples were degassed at 200 ℃ for 6 h. Thermal gravimetric (TGA) performance of specimens were conducted on Setaram Labsys Evo with a heating rate of 5 ℃/min under Argon atmosphere until 700 ℃. The concentrations of Li^+ and other cations were measured by optical emission spectrometer(ICP, iCAP6500 DUO, Thermo Fisher Scientific, America).

3 Results and discussion

3.1 Synthesis of $Li_{1.6}Mn_{1.6}O_4$-type precursor and LIS

TG curves of the Mn_2O_3 and $LiOH \cdot H_2O$ mixtures and the as-prepared $LiMnO_2$ intermediate are shown in Figs. 2(a) and 2(b), respectively. Under the Ar atmosphere, the reactant mixture of Mn_2O_3 and $LiOH \cdot H_2O$ began a solid-phase reaction at approximately 100 ℃ that ended at approximately 600 ℃. The total weight loss in this temperature range was approximately 22.26 %, almost identical to the theoretical value(–22.35%) from the chemical reaction($Mn_2O_3 + 2LiOH \cdot H_2O \rightarrow 2LiMnO_2 + 3H_2O\uparrow$). Further calcination of the as-obtained intermediate $LiMnO_2$ samples at high temperature in O_2 (Fig. 2(b)) led to an increase in the weight that increased with calcination temperature and reached a maximum at approximately 450 ℃. From room temperature to 450 ℃, this weight gain was approximately 8.56 % and is mainly attributable to the oxidation of Mn^{3+} ($4LiMnO_2 + O_2 \rightarrow 2.5\ Li_{1.6}Mn_{1.6}O_4$). Overall, TG analysis demonstrated the feasibility of preparing a $Li_{1.6}Mn_{1.6}O_4$-type precursor using Mn_2O_3 as a manganese source.

Compared with the standard characteristic diffractionpeak, those of S-$LiMnO_2$ and C-$LiMnO_2$ are in accordance with that of orthorhombic $LiMnO_2$ (JCPDS No. 35 – 0749). As shown in Fig. S1, the morphology of Mn_2O_3 (Fig. S2) had little influence on the evolution of their crystal structures. The obtained XRD patterns of spherical $Li_{1.6}Mn_{1.6}O_4$ (S-LMO), cubic $Li_{1.6}Mn_{1.6}O_4$ (C-LMO), and the corresponding spherical LIS (S - LIS) and cubic LIS

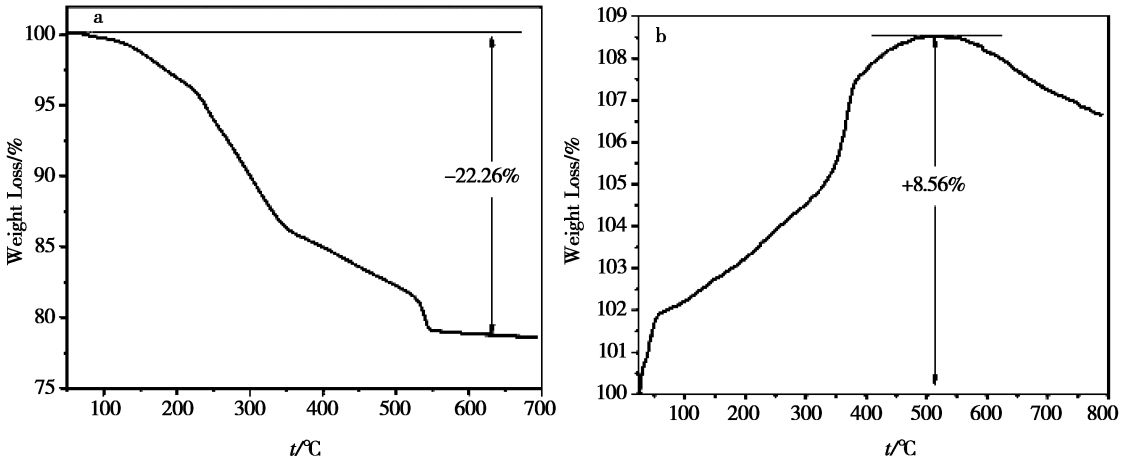

Fig. 2　TG curve of (a) Mn_2O_3 and $LiOH \cdot H_2O$ mixtures under Ar stepped at a rate of 10 ℃/min, and (b) $LiMnO_2$ under O_2 at a rate of 10 ℃/min

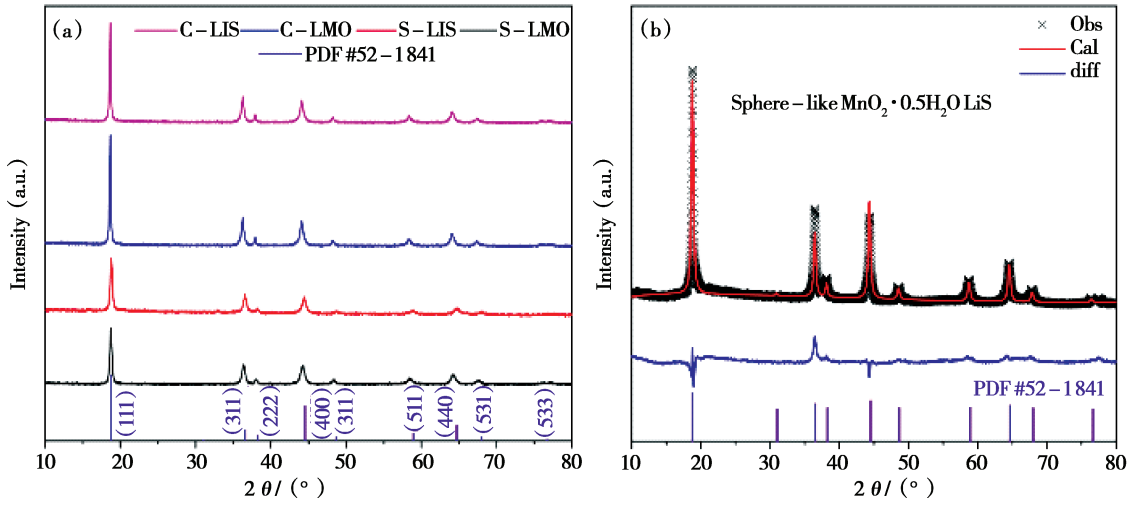

Fig. 3　(a) XRD patterns of as-obtained S-LMO, C-LMO, S-LIS, C-LIS and (b) XRD refinement pattern of as-obtained sphere-like LISs

(C-LIS) are shown in Fig. 3(a). The diffraction patterns of C-LMO and S-LMO both have eight typical peaks at 2θ = 18.7°, 36.3°, 38.1°, 44.2°, 48.3°, 58.4°, 64.1°, and 67.5°, corresponding to (111), (311), (222), (400), (331), (511), (440), and (531) crystal planes of cubic $Li_{1.6}Mn_{1.6}O_4$ (JCPDS card No. 52 − 1841) with the Fd3m space group[10-12]. The calculated cell parameters by Rietveld refinement (Fig. 3(b)) are $a = b = c = 0.8141$ nm and $\alpha = \beta = \gamma = 90°$, respectively. The lithium-rich spinel precursor $Li_{1.6}Mn_{1.6}O_4$ had a crystal structure similar to that of $LiMn_2O_4$ (Fig. S3(a)). Based on $LiMn_2O_4$, the lithium-rich precursor $Li_{1.6}Mn_{1.6}O_4$ could be formulated as $(Li)(Li)_{0.2}[Li_{0.4}Mn(IV)_{1.6}]O_4$, where 5/8 of the lithium atoms occupy the 8a sites of tetrahedrons, 1/4 occupy the 16d sites of octahedrons, and the remaining 1/8 move freely throughout the structure; this proposed formulation is detailed in Fig. S3(b).

The typical diffraction peaks of the S-LIS and C-LIS are displayed in Fig. 3(a). Briefly, compared with those of S-LMO and C-LMO, the characteristic peak intensities of C-LIS and S-LIS were slightly weakened, and their diffraction peak 2θ angles are shifted slightly to the right. Because the radius of H^+ is smaller than that of Li^+, exchanging Li^+ for H^+

caused the plane crystal space to become narrower, thereby shrinking the unit cell. However, based on the XRD refinement pattern of the as-obtained S-LIS (Fig. 3(b)), the face-centered cubic-phase spinel structure of the precursor was maintained, which indicates that the spinel crystal structure was not destroyed by acid elution of precursor and that the as-prepared LIS has good structural stability. Furthermore, introducing H^+ increased the – OH stretching and bending vibrations of S-LIS when compared with S-LMO, whereas the intensity and wavenumbers of the Mn-O asymmetric stretching vibration modes of the MnO_6 group did not drastically change, indicating that the Mn-O bands were maintained (Fig. S4), which is consistent with the above XRD results.

Fig. 4 displays FE-SEM images of C-LMO, S-LMO, C-LIS, and S-LIS, TEM images of S-LMO, S-LIS, and HRTEM images and corresponding SAED images (insert) of S-LMO and S-LIS. After high-temperature calcination, a solid-phase reaction occurred between Mn_2O_3 (C-Mn_2O_3 and S-Mn_2O_3) and LiOH, forming precursor $Li_{1.6}Mn_{1.6}O_4$ with cubic-like or sphere-like morphology (i. e., C-LMO and S-LMO, Figs. 4(a) and 4(c), respectively), demonstrating that the morphology of the reactant (Fig. S2) largely determines the shape of the products. The average diameter of C-LMO and S-LMO were 1.8 and 1.5 μm, respectively. After acid treatment, as depicted in Fig. 4(b) and (d), the as-prepared C-LIS and S-LIS maintained their cubic and spherical morphologies inherited from their corresponding Mn_2O_3 reactant and had an average size of 1.5 and 1.3 μm, respectively. The cell shrinkage caused by Li^+ and H^+ exchange during acid treatment, as concluded from XRD (see Fig. 3(a)), likely caused the size changes of the LISs. TEM images of the S-LMO and S-LIS are displayed in Figs. 4(e) and 4(f), respectively, to further trace the morphology and structure changes of S-LMO before and after acid treatment. These images demonstrate that S-LMO and S-LIS are porous and confirm the morphology and size observed from the FE-SEM images (Figs. 4(c) and 4(d)). In addition, the inter-planar spacings of the lattice planes shown in the HRTEM image (Fig. 4(g)) were 0.473 and 0.247 nm, which agree well with those of the (111) and (311) lattice planes of cubic $Li_{1.6}Mn_{1.6}O_4$, respectively. Moreover, the corresponding SAED pattern shown in the inset of Fig. 4(g) confirms the polycrystalline characteristic of the as-prepared samples. After acid treating, the inter-planar spacing of the (111) lattice plane of as-obtained S-LIS shrunk from its corresponding precursor (S-LMO) of 0.473 to 0.471 nm, which is mainly attributed to ion-exchange processes.

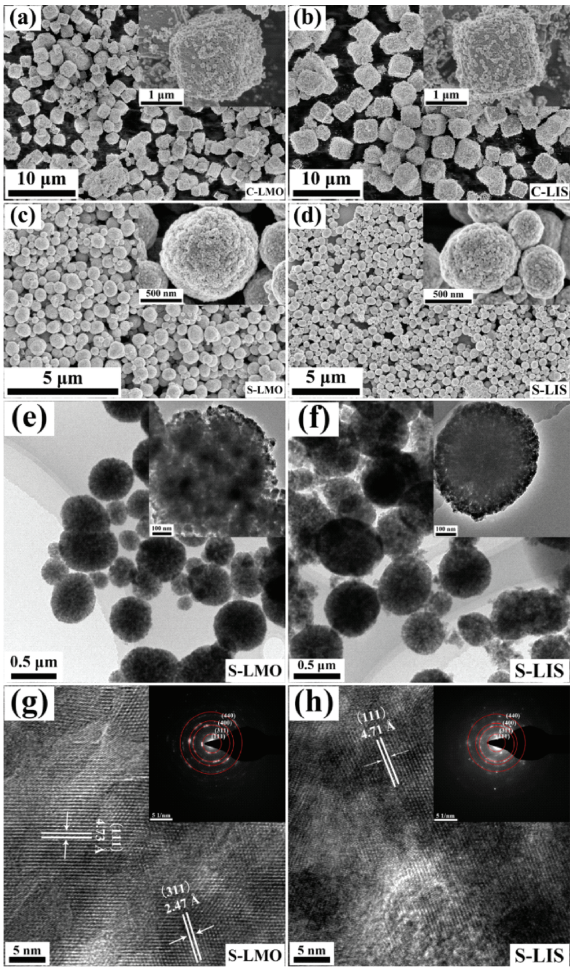

Fig. 4 (a – d) FE-SEM images of C-LMO, C-LIS, S-LMO, and S-LIS; (e – f) TEM images of S-LMO and S-LIS; (g – h) SAED images of S-LMO and S-LIS

Under the same desorption conditions, as shown in Figs. 5(a) and 5(b), C-LMO required approximately 80 more minutes than S-LMO to reach an Mn loss rate equilibrium (180 versus 100 min, respectively). The corresponding Li equilibrium desorption of S-LMO and C-LMO was 94.4% and 81.7%, respectively. Despite its higher Li desorption, S-LMO had a lower Mn loss than C-LMO. As the only difference between these two $Li_{1.6}Mn_{1.6}O_4$-type precursors is their morphology, morphology must influence their adsorption; this is discussed in more detail in the following sections.

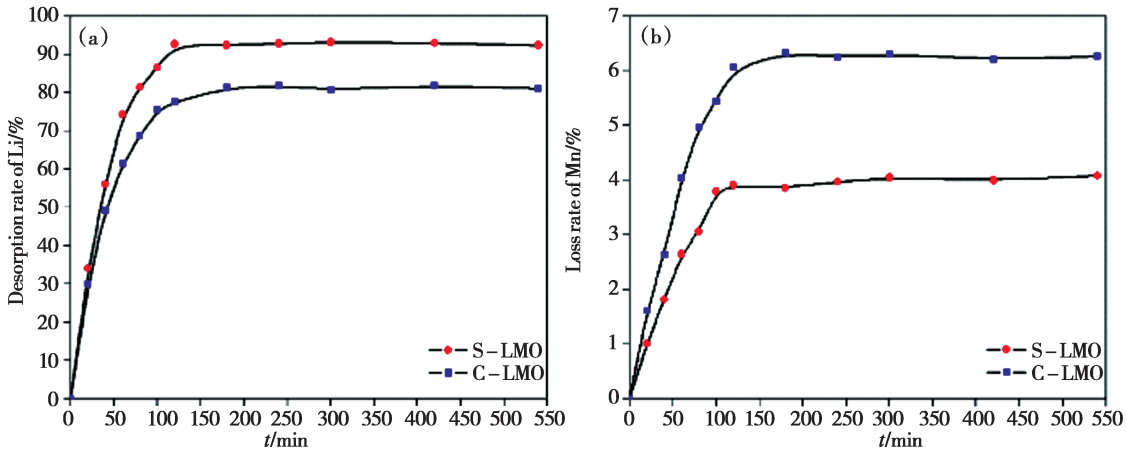

Fig. 5　(a) Li desorption rate and (b) Mn loss rate as a function of acid treating time of C-LMO and S-LMO

3.2　Adsorption performances of as-prepared LIS

The change in adsorption capacity of S-LIS and C-LIS with time is shown in Fig. 6(a). The adsorption capacity of S-LIS and C-LIS increased with adsorption time linearly until equilibrating after 25 h. The equilibrium adsorption capacities of S-LIS and C-LIS were approximately 25.94 and 42.46 mg/g under the same adsorption conditions, respectively, which is mainly related to their lithium desorption rate, as shown in Fig. 5(a). Moreover, the adsorption capacity of S-LIS was increased due to its high specific surface area (up to 42.495 m^2/g, as determined from the BET method, Fig. S5) and mesoporous characteristic (with a pore diameter of approximately 23.418 nm, Table S1). The experimental Li^+ adsorption data of the S-LIS was analyzed using pseudo-first-order and pseudo-second-order kinetic models (Equations (5) ~ (6)) to determine the adsorption mechanism and the rate constant of the adsorption process[20].

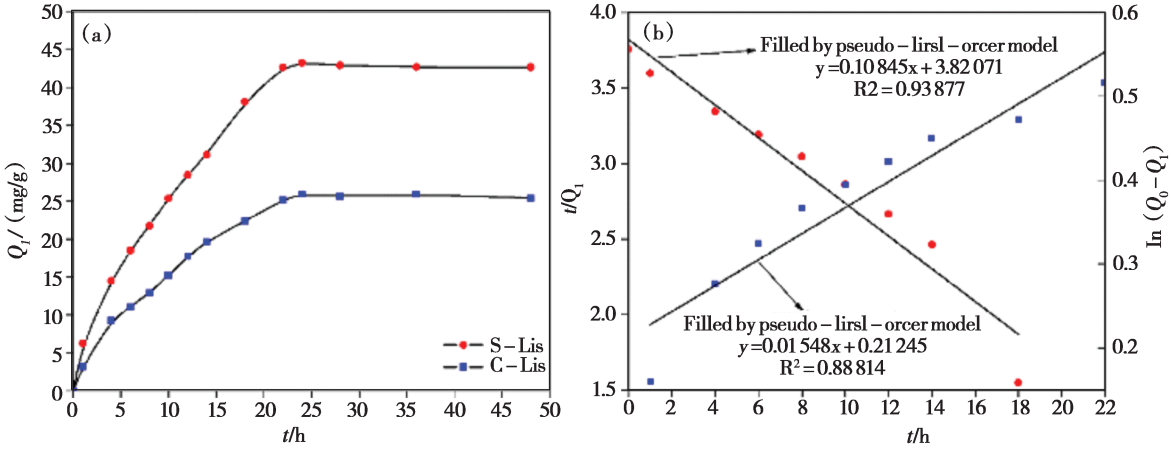

Fig. 6　(a) Adsorption of Li^+ ions into S-LIS and C-LIS as a function of time and (b) adsorption kinetic curves of S-LIS fitted with the pseudo-first-order and the pseudo-second-order models

$$\ln(Q_e - Q_t) = \ln Q_e - k_1 \times t \quad (5)$$

$$\frac{t}{Q_t} = \frac{1}{k_2} \times Q_e^2 + \frac{t}{Q_e} \quad (6)$$

where k_1 (min^{-1}) and k_2 ($mg \cdot g^{-1} \cdot min^{-1}$) are rate constants of pseudo-first-order and pseudo-second-order adsorption, respectively. Fig. 6 (b) shows the adsorption kinetic curves of S-LIS fitted with the two kinetic models, and the calculated parameters of adsorption kinetic models are given in Table 1. The correlation coefficient (R^2) of the pseudo-first-order model was higher than that of the pseudo-second-order model (0.93887 and 0.88814, respectively). Additionally, the calculated equilibrium adsorption capacity (Q_e) of the pseudo-first-order model (45.64 mg/g) was closer to the experimental value of 42.46 mg/g. Thus, the adsorption rate was described well by pseudo-first-order kinetics before reaching equilibrium. The calculated adsorption rate constant was 3.013×10^{-5} s^{-1}.

The influence of the initial concentration of Li^+ ions (C_0) on the adsorption capacity of the S-LIS was then further analyzed, as shown in Fig. 7 (a). When $C_0 < 100$ mg/L, Q_e of the Li^+ ions linearly increased with C_0. When $C_0 > 100$ mg/L, Q_e did not significantly increase further and remained around 42.46 mg/g. The adsorption isotherm of S-LIS was fitted by the Langmuir and Freundlich models (Equations (7) ~ (8)), respectively)[20-22].

Table 1 Adsorption rate constants obtained from the pseudo-first-order and pseudo-second-order kinetic models of Li^+ onto S-LIS

Pseudo-first-order model			Pseudo-second-order model		
k_1/h^{-1}	Q_e/(mg/g)	R^2	k_2/(mg/(g·h))	Q_e/(mg/g)	R^2
0.108 45	45.64	0.938 87	0.019 64	64.60	0.888 14

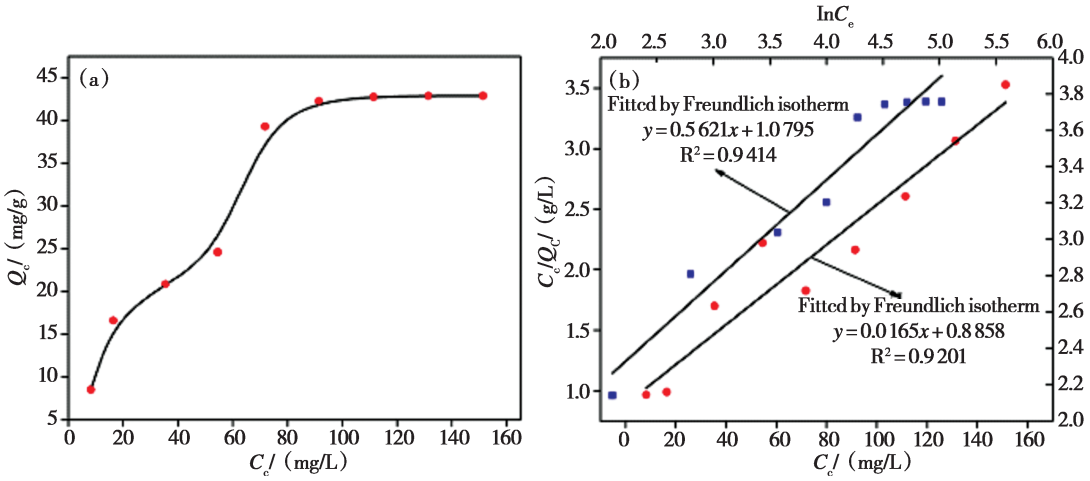

Fig. 7 (a) Adsorption equilibrium capacity of Li^+ onto S-LIS as a function of initial Li^+ ions concentration and (b) Adsorption curves fitted by Langmuir and Freundlich models, respectively

$$\frac{Ce}{Q_e} = \frac{1}{bQ_m} + \frac{Ce}{Q_m} \quad (7)$$

$$\ln Q_e = \ln K_F + \frac{1}{n}\ln C_e \quad (8)$$

where b (L/mg) is the Langmuir adsorption constant, K_F and n are the Freundlich constants related to the lithium adsorption capacity and the lithium interaction of the adsorbent, respectively, which can be calculated from the slope and intercept of the plot of $\ln Qe$ vs $\ln C_e$.

TheS-LIS adsorption isotherms fitted by Langmuir model and Freundlich models are shown in Fig. 7 (b), and the corresponding calculated parame-

ters are given in Table S2. As shown in Fig. 7(b), the simulated curve by Freundlich model shows higher correlation coefficient(R^2) about 0.9414 than that of Langmuir model($R^2 = 0.9201$), herein indicating that the Freundlich model is more suitable for analysing the adsorption experimental data. Furthermore, the calculated Freundlich constant n is 1.78, indicating that the adsorption of Li^+ on as-prepared adsorbent is a multilayer physical adsorption process.

Asdisplayed in Fig. 8(a), solution pH obviously effects the adsorption capacity of S-LIS. Generally, the adsorption capacity of S-LIS toward Li^+ is below 5 mg/g in acidic environment and changes little with pH. Once the S-LIS works in an alkaline solution, Q_e sharply increases with pH, which is mainly attributed to the deprotonation process of S-LIS between its exchanged H^+ on porous surface with Li^+ during ion-exchange reaction and OH^- in solution. More, Fig. 8(b) confirms that, Li^+ adsorption capacity of S-LIS increases with temperature, which indicates the endothermic and diffusion-controlled Li^+ uptake nature of this sorption process[23].

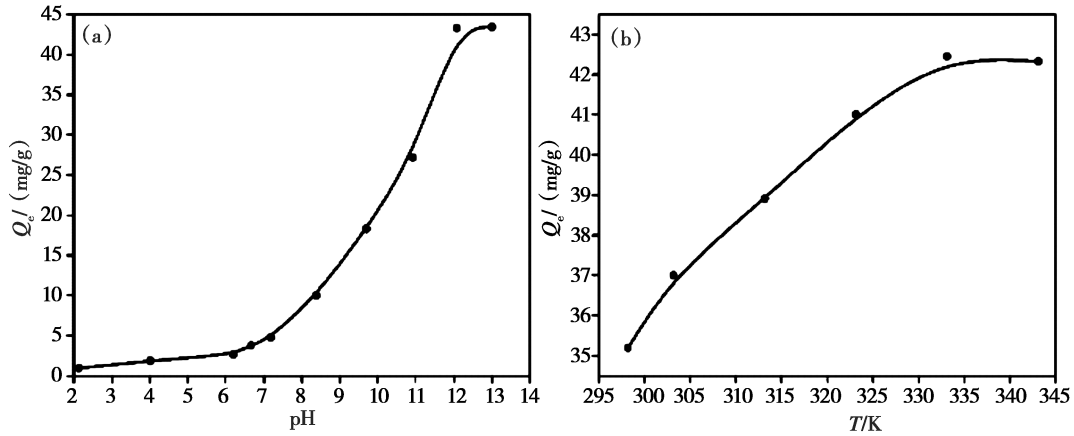

Fig. 8　Effects of(a) pH and(b) temperature on adsorption capacity of S-LIS

Selectivity experiments were then performed to clarify the influence of co-existing cations on Li^+ adsorption, such as Na^+, K^+, and Ca^{2+}; the results are summarized in Fig. 9(a) and Table 2. The designed S-LIS demonstrated high selectivity, with a Q_e of Li^+ of 42.009 mg/g and nearly no adsorption of any other cation. Additionally, the concentration coefficient (C_F) and distribution coefficient (K_d) of Li^+ were higher than those of other cations; further, the order of the calculated coefficient of specificity (α_{Me}^{Li}) of S-LIS toward different cations was $Li^+ > Na^+ > K^+ > Mg^{2+} > Ca^{2+}$. Thus, the S-LIS was concluded to have good selectivity toward Li^+.

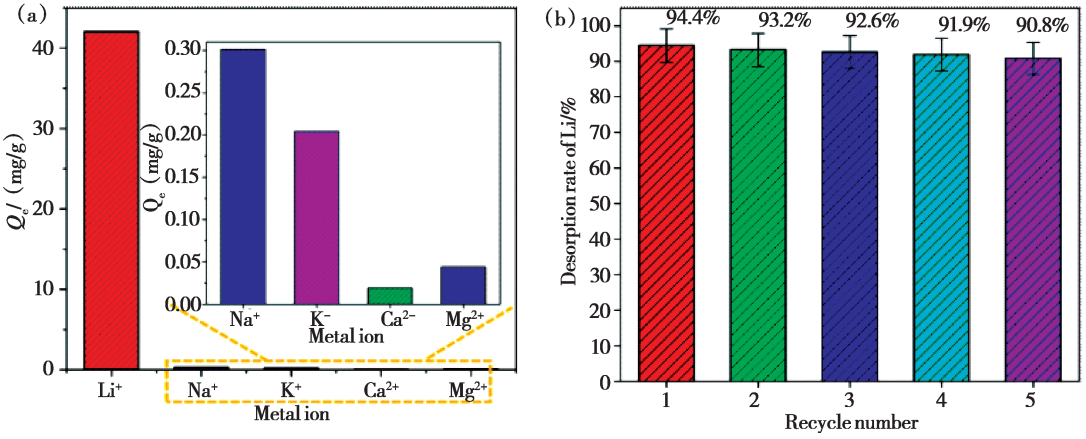

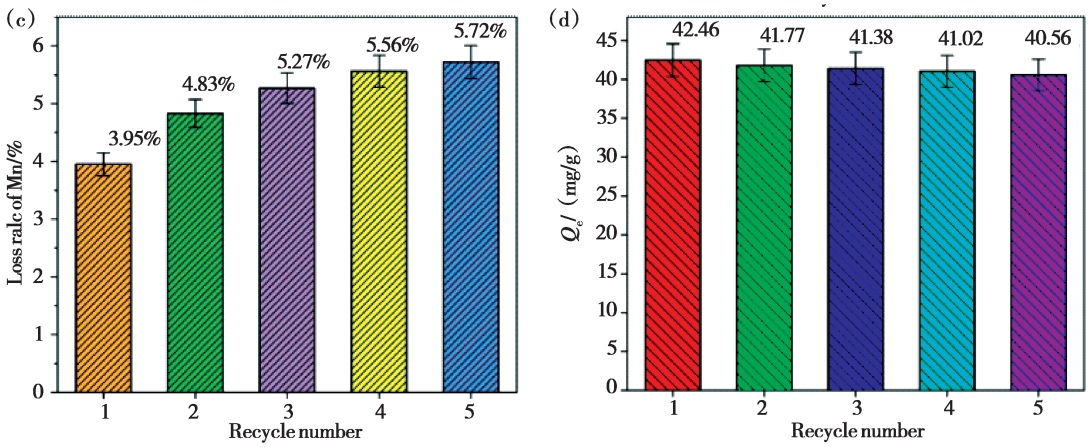

Fig. 9 (a) Adsorption capacity of various metal ions on S-LIS, (b) desorption rate of Li^+, (c) loss rate of Mn, and (d) Li^+ adsorption capacity for the first five desorption-adsorption cycles of S-LIS

After adsorption, the adsorbent was regenerated by acid treatment, and adsorption was repeated four times to characterize the cyclical performance; results are shown in Figs. 9(b) ~9(d). By the fifth adsorption-desorption cycle, the adsorption capacity of regenerated S-LIS decreased from 42.46 to 40.56 mg/g, thereby maintaining a desorption >90% and averaging an adsorption capacity fade of only 0.38 mg/g rate with each cycle. This loss is due to the gradual increase in the dissolution of Mn from 4.0% to 5.3% with increasing adsorption-desorption cycles caused by the Jahn-Teller distortion of Mn^{3+}[24-26].

Table 2 Calculated Li^+ adsorption selectivity parameters on S-LIS

Metal ions	C_0/(mg/L)	C_e/(mg/L)	Q_e/(mg/g)	C_F/($\times 10^{-3}$ L/g)	K_d/(mL/g)	α_{Me}^{Li}
Li^+	100.146	91.482	42.009	419.478	459.21	1
Na^+	100.785	100.723	0.301	2.987	2.98	154.09
K^+	100.211	100.169	0.204	2.036	2.03	226.21
Ca^{2+}	100.575	100.571	0.019	0.193	0.19	2416.89
Mg^{2+}	100.201	100.192	0.044	0.439	0.44	1043.66

3.3 Preparing and working mechanism of S-LIS

As the Li^+ adsorption of the as-prepared S-LIS detailed above demonstrate that the valance state of Mn in the precursor and target adsorbent plays a critical role, XPS was employed to clarify the formation and working mechanisms of S-LIS. The obtained XPS Mn 2p spectrum of S-LMO is shown in Fig. 10(a), where the peaks at 653.8 and 642 eV are assigned to Mn $2p_{1/2}$ and Mn $2p_{3/2}$, respectively. The Mn $2p_{3/2}$ spectrum fitted by CasaXPS software (NIST Standard Reference Database 20, Version 4.1, online) is depicted in Fig. 10(b). The two distinctive peaks in the fitted Mn $2p_{3/2}$ spectrum located at 642.2 and 643.2 eV are attributable to the Mn^{3+}-O and Mn^{4+}-O bonds, respectively[24-26], and the calculated Mn^{3+} ratio is approximately 30%, according to the area of the fitted curves. According to crystal field theory, Mn^{3+} is in a high-spin state and possesses a d^4 electronic configuration, whereas Mn^{4+} is in a low-spin state and possesses a d^3 electronic config-

uration; they are both in the octahedral field of an oxygen framework[27,28]. The octahedral field enables the 5*d* orbits of manganese to be split into five lower-energy orbits, comprising two e_g orbits and three t_{2g} orbits. Therefore, the three *d* electrons in Mn^{4+} are stable, whereas the extra electron in Mn^{3+} is more active, thereby causing the so-called Mn^{3+} disproportion ($2Mn^{3+} \leftrightarrow Mn^{4+} + Mn^{2+}$)[29-31]. Additionally, this excess electron can freely move in solid materials and is easily attracted to free Li^+, as shown in Fig. 10 (c). During the acid treating of the $Li_{1.6}Mn_{1.6}O_4$-type precursor, free Li^+ dissolved into solution may capture adjacent electrons by part of Mn^{4+} to form dissolvable Mn^{2+}. Mn^{3+} is thus further oxidized into Mn^{4+} and remains in the structure to stabilize its framework. Finally, structural Li^+ is replaced by H^+ in solution, thus forming $MnO_2 \cdot 0.5H_2O$ LISs ($5Li_{1.6}Mn_{1.6}O_4 + 8H^+ \rightarrow 8MnO_2 \cdot 0.5H_2O + 8Li^+$).

The proposedworking mechanism of the as-prepared adsorbent is summarized in Fig. 11. Once the $MnO_2 \cdot 0.5H_2O$ adsorbent is added into the Li^+-containing solution, deprotonation promotes the H^+ in the surface -OH groups (Fig. S4) to migrate out of the adsorbent framework and to combine with OH^- in solution, thus inserting Li^+ into the main body of the adsorbent[23,30]. This process may be accelerated by intensifying the concentration of OH^-; thus, pH and temperature influence adsorption performance (Fig. 8). The solution-based Li^+ then intercalates into the vacant sites caused by the deprotonated H^+. The lithiation process is motivated by the ion-exchange reaction between H^+ and Li^+ and thus transforms the adsorbent $MnO_2 \cdot 0.5H_2O$ into its corresponding precursor, $Li_{1.6}Mn_{1.6}O_4$ ($8MnO_2 \cdot 0.5H_2O + 8Li^+ \rightarrow 5Li_{1.6}Mn_{1.6}O_4 + 8H^+$). As discussed above, the regenerated $Li_{1.6}Mn_{1.6}O_4$ could be treated by acid again to form $MnO_2 \cdot 0.5H_2O$.

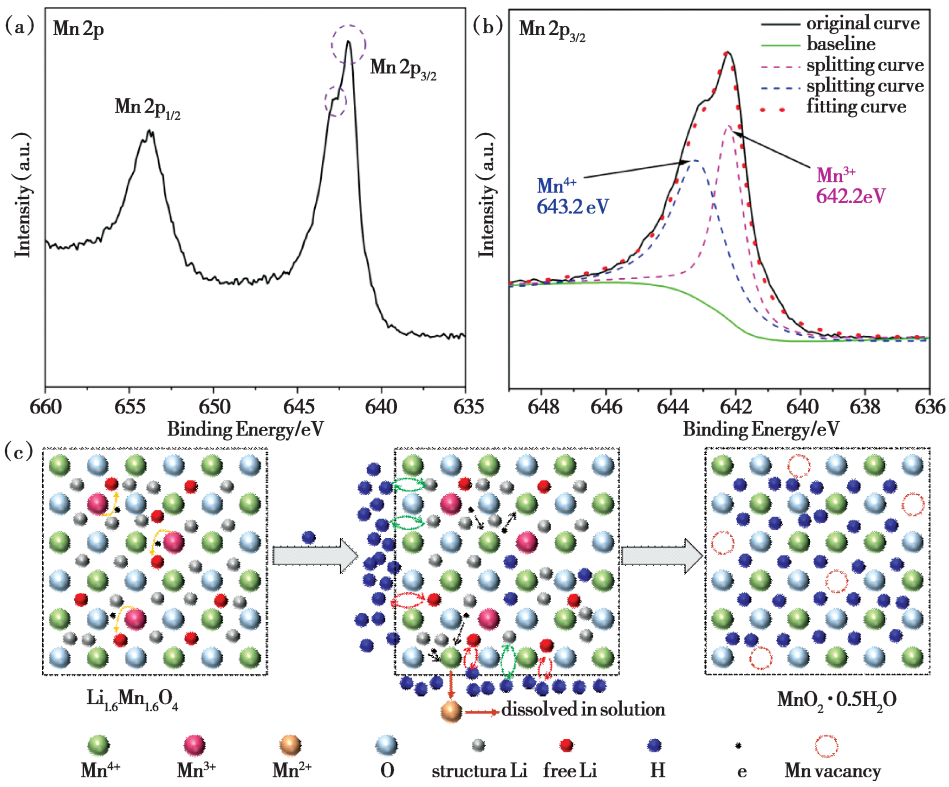

Fig. 10　(a) High-resolution XPS Mn 2p spectrum of as-prepared spherical $Li_{1.6}Mn_{1.6}O_4$, (b) fitted splitting curves of Mn $2p_{3/2}$, and (c) schematic of $MnO_2 \cdot 0.5H_2O$ preparation by adsorbent

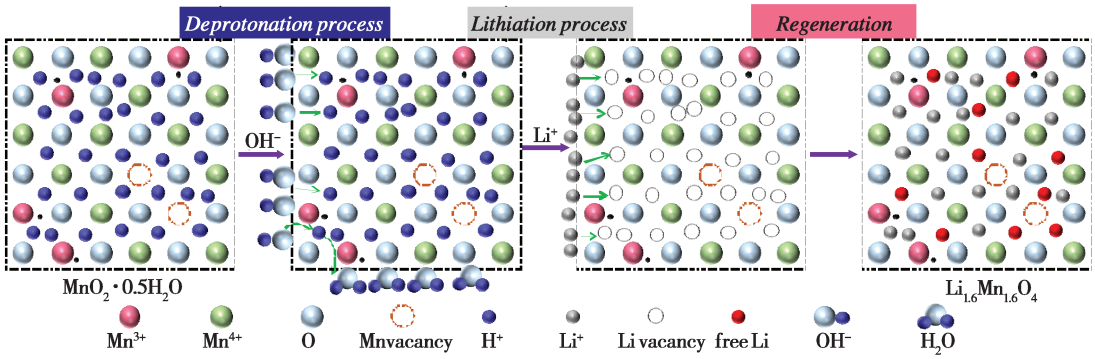

Fig. 11 Schematic illustration of adsorption mechanism of $MnO_2 \cdot 0.5H_2O$ LISs

4 Conclusions

A porous $Li_{1.6}Mn_{1.6}O_4$-type adsorbent $MnO_2 \cdot 0.5H_2O$ with a spherical morphology (i. e. , S-LIS) was successfully synthesized to recover Li^+ from solution via a simple two-step solid-phase method employing morphology-controlled Mn_2O_3 and commercial $LiOH \cdot H_2O$ as starting materials. The results presented here confirm that the morphology, specific surface area, and pore diameter influence the adsorption of the as-prepared adsorbents, especially S-LIS. The as-prepared S-LIS has a higher Li^+ adsorption capacity (42. 46 mg/g) than C-LIS with a similar average diameter did, which is thus attributable to its spherical morphology. The adsorption of Li^+ on the prepared S-LIS was explained by the Freundlich isotherm and pseudo-first-order kinetics models. Further, surface deprotonation and lithiation processes motivated by ion-exchange reactions begin the adsorption process of the solid adsorbent powder from an aqueous solution.

References:

[1] Tarascon J M, Armand M. Issues and challenges facing rechargeable lithium batteries[J]. Nature, 2001, 414(6861): 359 – 367.

[2] Winter M, Barnett B, Xu K. Before Li ion batteries[J]. Chemical Reviews, 2018, 118(23): 11433 – 11456.

[3] Lu L, Han X, Li J, *et al*. A review on the key issues for lithium-ion battery management in electric vehicles[J]. Journal of Power Sources, 2013(226): 272 – 288.

[4] Huang S, Cao P, Wang C, *et al*. Fabrication of a High-Strength Lithium Disilicate Glass-Ceramic in a Complex Glass System [J]. Journal of Asian Ceramic Societies, 2013, 1(1): 46 – 52.

[5] Tyrsa V E, Burtseva L P. Generation of thermonuclear energy by fusing hydrogen and lithium atoms[J]. Technical Physics, 2003, 48(7): 807 – 812.

[6] Karki K, Epstein E, CHO J H, *et al*. Lithium-assisted electrochemical welding in silicon nanowire battery electrodes[J]. Nano Letters, 2012, 12(3): 1392 – 1397.

[7] Zhao X, Zhang Q, Wu H, *et al*. Extraction of lithium from salt lake brine[J]. Progress in Chemistry, 2017, 29(7): 796 – 808.

[8] Yang S, Zhang F, Ding H, *et al*. Lithium Metal Extraction from Seawater[J]. Joule, 2018, 2(9): 1648 – 1651.

[9] Wang L, Meng C G, Ma W. Study on Li^+ uptake by lithium ion-sieve via the pH technique[J]. Colloids and Surfaces A: Physicochemical and Engineering Aspects, 2009, 334(1): 34 – 39.

[10] Song J F, Nghiem L D, Li X M, *et al*. Lithium extraction from Chinese salt-lake brines: opportunities, challenges, and future outlook[J]. Environmental Science-Water Research & Technology, 2017, 3(4): 593 – 597.

[11] Epstein J A, Feist E M, Zmora J, *et al*. Extraction of Lithium from the Dead Sea[J]. Hydrometallurgy, 1981, 6(3): 269 – 275.

[12] Kenjiro Y, Tetsutaro Y, Kentaro K, *et al*. The Recovery of Lithium from Geothermal Water in the Hatchobaru Area of Kyushu, Japan[J]. Bulletin of the Chemical Society of Japan, 1983, 56(8): 2490 – 2498.

[13] Zandevakili S, Ranjbar M, Ehteshamzadeh M. Recovery of lithium from Urmia Lake by a nanostructure MnO_2 ion sieve[J]. Hydrometallurgy, 2014(149): 148 – 152.

[14] Dang V D, Steinberg M. Preliminary Design and Analysis of Recovery of Lithium from Brine with the Use of a Selective Extractant[J]. Energy, 1978, 3(3): 325 – 336.

[15] Xiao J, Nie X, Sun S, *et al*. Lithium ion adsorption-desorption properties on spinel $Li_4Mn_5O_{12}$ and pH-dependent ion-ex-

change model [J]. Advanced Powder Technology, 2015, 26 (2): 589 – 594.

[16] Chitrakar R, Kanoh H, Miyai Y, *et al*. A New Type of Manganese Oxide ($MnO_2 \cdot 0.5H_2O$) Derived from $Li_{1.6}Mn_{1.6}O_4$ and Its Lithium Ion-Sieve Properties [J]. Chemistry of Materials, 2000, 12(10): 3151 – 3157.

[17] Liu L, Zhang H, Zhang Y, *et al*. Lithium extraction from seawater by manganese oxide ion sieve $MnO_2 \cdot 0.5H_2O$ [J]. Colloids and Surfaces A: Physicochemical and Engineering Aspects, 2015(468): 280 – 284.

[18] Shi X C, Zhou D F, Zhang Z B, *et al*. Synthesis and properties of $Li_{1.6}Mn_{1.6}O_4$ and its adsorption application [J]. Hydrometallurgy, 2011, 110(1 – 4): 99 – 106.

[19] Qi G, Hai C, Shen Y, *et al*. Synthesis of mono-dispersed mesoporous Mn_2O_3 powders with micro-nanostructure for removing Congo red dye from aqueous solution [J]. Advanced Powder Technology, 2019, 30(5): 930 – 939.

[20] Zhu G R, Wang P, Qi P F, *et al*. Adsorption and desorption properties of Li^+ on PVC – $H_{1.6}Mn_{1.6}O_4$ lithium ion-sieve membrane [J]. Chemical Engineering Journal, 2014 (235): 340 – 348.

[21] Jing Z H, Zhan J H. Fabrication and Gas-Sensing Properties of Porous ZnO Nanoplates [J]. Adv Mater, 2008, 20(23): 4547 – 4551.

[22] Hu J S, Ren L L, Guo Y G, *et al*. Mass production and high photocatalytic activity of ZnS nanoporous nanoparticles [J]. Angew Chem Int Ed Engl, 2005, 44(8): 1269 – 73.

[23] Stranick M A. Mn_2O_3 by XPS [J]. Surface Science Spectra, 1999, 6(1): 39 – 46.

[24] Militello M C, Gaarenstroom S W. Lithium Manganese Oxide ($LiMn_2O_4$) by XPS [J]. Surface Science Spectra, 2002, 8(3): 207 – 213.

[25] Salavati M, Mohandes F, Davar F, *et al*. Fabrication of chain-like Mn_2O_3 nanostructures via thermal decomposition of manganese phthalate coordination polymers [J]. Applied Surface Science, 2009, 256(5): 1476 – 1480.

[26] Cao H, Wu X, Wang G, *et al*. Biomineralization Strategy to α-Mn_2O_3 Hierarchical Nanostructures [J]. The Journal of Physical Chemistry C, 2012, 116(39): 21109 – 21115.

[27] Xu X, Chen Y, Wan P, *et al*. Extraction of lithium with functionalized lithium ion-sieves [J]. Progress in Materials Science, 2016(84): 276 – 313.

[28] Hunter J C. Preparation of a new crystal form of manganese dioxide: λ-MnO_2 [J]. Journal of Solid State Chemistry, 1981, 39 (2): 142 – 147.

[29] Singh G, Gupta S L, Prasad R, *et al*. Suppression of Jahn-Teller distortion by chromium and magnesium doping in spinel $LiMn_2O_4$: A first-principles study using GGA and GGA + U [J]. Journal of Physics and Chemistry of Solids, 2009, 70(8): 1200 – 1206.

[30] Iqbal M J, Ahmad Z. Electrical and dielectric properties of lithium manganate nanomaterials doped with rare-earth elements [J]. Journal of Power Sources, 2008, 179(2): 763 – 769.

[31] Gao A, Sun Z, Li S, *et al*. The mechanism of manganese dissolution on $Li_{1.6}Mn_{1.6}O_4$ ion sieves with HCl [J]. Dalton Transactions, 2018, 47(11): 3864 – 3871.

球形 $MnO_2 \cdot 0.5H_2O$ 提锂性能及其机理研究

张果泰[1,2], 漆贵财[1,2], 海春喜[1], 周　园[1]

(1. 中国科学院青海盐湖研究所, 盐湖资源综合高效利用重点实验室, 青海省盐湖资源化学重点实验室, 青海 西宁　810008; 2. 中国科学院大学, 北京　100049)

摘　要: 考察了形貌对尖晶石型锂离子筛吸附剂 $MnO_2 \cdot 0.5H_2O$ 吸附性能的影响。实验证明, 反应物 Mn_2O_3 的形貌在很大程度上决定了前驱体及其吸附剂的形貌。采用 XRD、SEM、TEM、FT-IR、XPS 和 N_2 吸附—解吸等温线等对样品进行了表征。表征和吸附实验结果表明, 与立方形锂离子筛相比, 球形锂离子筛具有较高的吸附容量 (42.46 mg/g), 同时对溶液中的 Li^+ 具有较高的选择性。表面脱质子和离子交换过程的共同作用增强了离子筛型吸附剂的提锂 Li^+ 性能。此外, 本文对 $Li_{1.6}Mn_{1.6}O_4$ 与 $MnO_2 \cdot 0.5H_2O$ 的吸附—解吸机理进行了解释。

关键词: 尖晶石型 $Li_{1.6}Mn_{1.6}O_4$; $MnO_2 \cdot 0.5H_2O$; 锂回收; 吸附容量; 吸脱附机制